IEEE Access
Multidisciplinary | Rapid Review | Open Access Journal

Received September 9, 2019, accepted September 26, 2019, date of publication September 30, 2019,
date of current version October 10, 2019.

Digital Object Identifier 10.1109/ACCESS.2019.2944681

Wideband MIMO Antenna Array Covering 3.3–7.1 GHz for 5G Metal-Rimmed Smartphone Applications

QINYI CAI[1], YIXIN LI[2], XUGANG ZHANG[1], AND WENHUI SHEN[1]
[1]School of Communication and Information Engineering, Shanghai University, Shanghai 200444, China
[2]School of Electronic and Information Engineering, South China University of Technology, Guangzhou 510641, China

Corresponding author: Wenhui Shen (haomeni@163.com)

ABSTRACT A wideband 8-antenna Multiple-Input Multiple-Output (MIMO) array covering 3.3–7.1 GHz for Fifth-Generation (5G) sub-7 GHz and New Radio Unlicensed (NR-U) applications in metal-rimmed smartphones is presented in this paper. In this design, the open slot loaded metal rim is directly fed by microstrip line. Hybrid Inverted-F Antenna (IFA) and slot modes are generated. Utilizing impedance matching and reactance loading, the two modes are moved and combined, so as to achieve size reduction and wideband coverage. The size of the ground slot (clearance) is only 12.4 mm × 1.5 mm ($0.136\,\lambda \times 0.016\,\lambda$ at 3.3 GHz). The proposed MIMO antenna array is fabricated and measured. Results show that in the desired wide frequency band, the proposed design can achieve desirable antenna performances, including isolation >11 dB, total efficiency >47%, and calculated Envelope Correlation Coefficient (ECC) <0.09. Besides, antenna gain, radiation pattern and calculated ergodic channel capacity are demonstrated as well. The proposed metal-rim-integrated MIMO antenna array features small size, simple structure and wide bandwidth. It can be a good application-oriented design in next-generation 5G mobile communication.

INDEX TERMS 5G communication, metal-rimmed smartphone, MIMO antenna, wideband.

I. INTRODUCTION

With the increasing demand for high transmission rate, Fifth-Generation (5G) mobile communication is gradually coming into our sight. Owing to the ability of obtaining higher channel capacity than traditional Fourth-Generation (4G) antennas, Multiple-Input Multiple-Output (MIMO) antenna arrays are deemed to have a broad prospect for 5G mobile terminal applications.

According to Qualcomm's presentation regarding 5G New Radio (NR), a global snapshot of 5G middle band allocation is given in Fig. 1 [1]. Generally speaking, the 5G middle band can be categorized into licensed band, unlicensed/shared band, and existing band. Among them, the existing frequency band mainly refers to Long Term Evolution (LTE) band 41 (2.496–2.69 GHz), which belongs to sub-3 GHz spectrum, and is part of 4G high band. Above 3 GHz, multiple licensed and unlicensed bands form a consecutive wide bandwidth of 3.3–5 GHz, which has been identified by 3rd Generation Partnership Project (3GPP) as the combination of 5G NR bands N77 (3.3–4.2 GHz), N78 (3.3–3.8 GHz) and N79 (4.4–5 GHz) [2]. The NR bands N77/N78/N79 together with the unlicensed LTE band 46 (5.15–5.925 GHz) have been recognized as vital components of 5G sub-6 GHz spectrum. The above-mentioned frequency bands have been intensively studied in some previous works [3]–[8], [11], [12]. Note that although LTE band 46 is not incorporated in the Qualcomm's presentation for the moment, it is considered as an important unlicensed band for 5G New Radio Unlicensed (NR-U) applications [13]. However, to realize the future prospective of multiband 5G NR-U, more possible unlicensed bands need to be supported. Very recently, Federal Communications Commission (FCC) and Confederation of European Posts and Telecommunications (CEPT) have started initiatives to investigate potentialities for deployment of International Mobile Telecommunications (IMT) services in 5.9–7.1 GHz (to be specific, US 5.9–7.1 GHz, and EU 5.9–6.4 GHz), with considerations for all or part of this range being made available for unlicensed operation [14]. This situation signifies that 5G sub-6 GHz will evolve into 5G sub-7 GHz in the near future.

For terminal antennas, multiband and wideband technique is the key to realize consecutive wideband coverage across the

The associate editor coordinating the review of this manuscript and approving it for publication was Ali Afana.

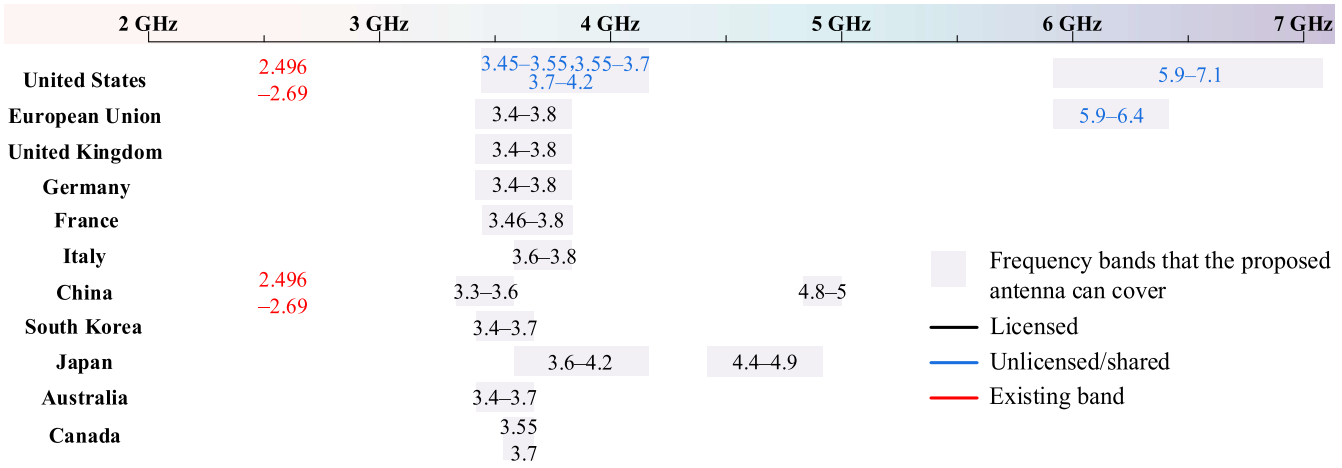

FIGURE 1. Allocation of global 5G spectrum in middle band (excerpted from Qualcomm's 5G NR presentation [1]).

entire sub-7 GHz spectrum. Over the years, a large number of multiband and wideband MIMO terminal antennas have been reported, and some corresponding bandwidth enhancement techniques have also been devised. It is a common technique to generate new resonance modes by employing multiple radiators. In [3], a dual-band 8-port antenna array has been presented. Each antenna element can cover LTE bands 42/46, which are attained by an L-shaped slot and a side-edge printed monopole, respectively. In [4], a 12-port MIMO antenna array operating in LTE bands 42/43/46 has been studied, of which the π-shaped element generates an additional resonance by adding a new branch. Adding new radiators is a convenient way to achieve multiband operation, but this method will, to a certain extent, increase antenna size. In recent years, matching circuit has also been regarded as a handy yet effective approach to enhance bandwidth. An 8-antenna metal-rim-integrated MIMO array analyzed in [5] can operate in both LTE band 41 and 3.3–3.7 GHz band through embedding two capacitors into radiation branches. A MIMO antenna based on Composite Right/Left-Handed Transmission Line (CRLH-TL) [6] utilizes a band-stop matching circuit to create a new resonance at low frequency. However, matching network will inevitably bring additional insertion loss. Also, for 5G MIMO arrays with 8 or more antenna elements integrated, too many lumped elements will make the design costly. Moreover, coupled feeding is also a feasible bandwidth enhancement technology [7], [8]. But this method is not always suitable for the mass production of antennas, as the bandwidth potential could be sensitive to the slight variation of the coupled section. In addition, multifeed structure has been used to expand bandwidth for 4G MIMO antennas [9], [10]. However, this method also lacks some practicability for 5G MIMO antenna design, as the growing number of feeding structures will lead to a steep rise in complexity.

Different from the methods mentioned above, mode manipulation technique refers to enhancing bandwidth through controlling and combining the resonance modes of a single radiating aperture. In general, the procedure of mode manipulation includes three steps: mode generation, mode adjustment and mode combination. First, one needs to select a proper radiating aperture, and excites its multiple resonance modes simultaneously. Here, whether heterogeneous mode (e.g., parasitic mode) or homogeneous mode (e.g., high-order mode) could be excited, as long as it has certain potential to cover the desired operation bandwidth. At this point, the excited modes could have relatively poor impedance matching and undesired resonance frequency. Therefore, afterwards, the modes should be fine adjusted, mainly to improve impedance matching, and shift resonance frequency without increasing antenna size. In this step, a 6-dB return loss level is generally acceptable for most 5G mobile handset antennas operating in middle band. The modes are usually shifted towards lower frequency, as this operation could reduce the electrical size of the aperture. Lastly, multiple resonance modes are combined, to form a consecutive wide operation bandwidth. Here, tuning frequency ratio is the key factor. Usually, the high-band modes are tuned towards lower frequency with the low-band modes kept still, in order to realize mode combination and antenna miniaturization simultaneously. Some exemplary designs using mode manipulation and mode combination can be found in [11], [12], [15], [16], in which consecutively operated wideband slot or loop antennas are introduced. In summary, in contrast with the above-mentioned methods, wideband antenna design based on mode manipulation has advantages of simple structure, low insertion loss and small size (as the number of radiating apertures is usually reduced). If the resonance modes can be controlled subtly, this method will be a good candidate for MIMO antennas supporting a consecutive wide bandwidth.

In this paper, for the first time, a wideband 8-element MIMO handset antenna array that consecutively covers 3.3–7.1 GHz is proposed. The very wide operating bandwidth of the proposed work can cover almost all

licensed and unlicensed 5G bands in sub-7 GHz, including three NR bands (N77/N78/N79), and two NR-U bands (5.15–5.925 GHz/5.9–7.1 GHz), as indicated by the shaded area in Fig. 1. Furthermore, to meet the industrial demand, the proposed antenna array is integrated into metallic rim platform. The proposed design successfully realizes wideband coverage and antenna miniaturization from two aspects: impedance matching and reactance loading. Each antenna element, which consists of a narrow rectangular slot etched on the ground (ground clearance) and a side-edge etched gap, could generate two modes, i.e., Inverted-F Antenna (IFA) mode and slot mode, at one time. The side-edge metal rim is directly fed through microstrip feeding line, thus it could function as radiator (IFA section). By means of meandered impedance transformer and tuning stub, the two diverse modes can be moved and merged, resulting in a wide bandwidth. The reflection coefficients of the proposed antenna array are less than −6 dB across 3.3–7.1 GHz, with isolation greater than 11 dB. Besides S parameters, radiation performances (radiation pattern, total efficiency and realized gain) and MIMO performances (ECC and ergodic channel capacity) are also investigated. The measured results of this work are compared with previous works, to highlight the novelty of the proposed work. CST Microwave Studio Version 2018 is used to obtain the simulated results.

II. PROPOSED 8-ANTENNA ARRAY

A. ANTENNA ARRAY STRUCTURE

Fig. 2 illustrates the proposed wideband (3.3–7.1 GHz) MIMO antenna array for 5G metal-rimmed smartphones. As we can see from Fig. 2(a), an FR4 substrate (relative permittivity = 4.4 and loss tangent = 0.025) whose size is 150 mm × 75 mm × 0.8 mm is elected as the main circuit board of smartphone. A metal ground is printed on the back surface. Four side frames (height = 7 mm) are placed vertically, and electrically connected to the edges of the ground plane. The inner sides of the frames are copper-plated, so as to simulate the four metal rims of smartphone. Eight centrosymmetric antenna elements (Ant 1 to Ant 8) are arranged along the two long edges. As shown in Fig. 2(b), the metal ground is located 1 mm higher than the bottom of the metal rims, in order to reserve sufficient space for display module.

B. ANTENNA ELEMENT STRUCTURE

The top view of the antenna element is shown in Fig. 2(c), which clearly reveals its specific structure. There is a narrow rectangular slot clearance (12.4 mm × 1.5 mm) etched on the metal ground. A rectangular gap is etched on the long side-edge metal rim, which forms an L-shaped slot aperture together with the clearance. Although the side frame is etched, in fact, most antenna designs with integrated metal rims need to be sliced reasonably [5], [9]. For engineering applications, using nano injection and nano molding technologies, plastic can be filled into the gap to ensure the integrity and mechanical strength of the frame. On the front

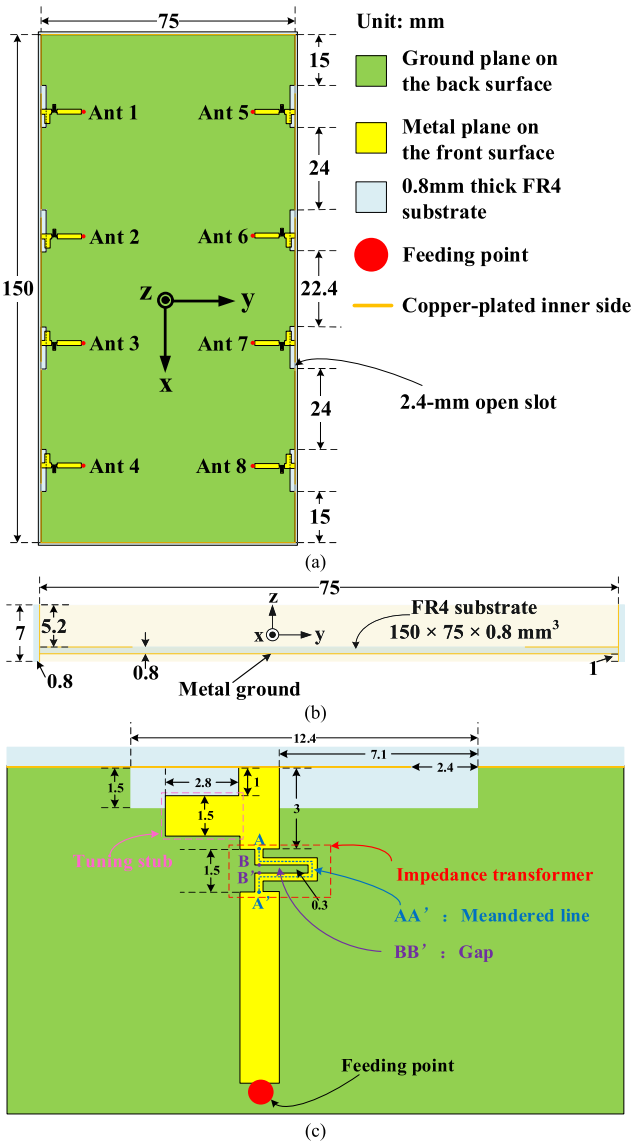

FIGURE 2. (a) Structure of the proposed antenna array, (b) Side view of the antenna array, (c) Top view of the antenna element.

surface of the substrate, a microstrip line is electrically connected to the inner side of the metal rim to feed the antenna element. A shunt tuning stub, which can be seen as a capacitively loaded tuner, is placed on the left side of the feeding line. Along the feeding strip, there is a narrow meandered line (width = 0.3 mm) joining the straight microstrip at points A and A'. In this design, it functions as an impedance transformer. Because the size of the clearance is only 12.4 mm × 1.5 mm (0.136 λ × 0.016 λ at 3.3 GHz), the proposed antenna element is suitable for application in the limited area between the display module and the metal rim. Further principle analysis of the antenna element will be given in Section III.

C. SIMULATED S-PARAMETER OF THE ANTENNA ARRAY

Simulated S parameters of the proposed MIMO antenna array are depicted in Fig. 3. Because of the symmetric placements

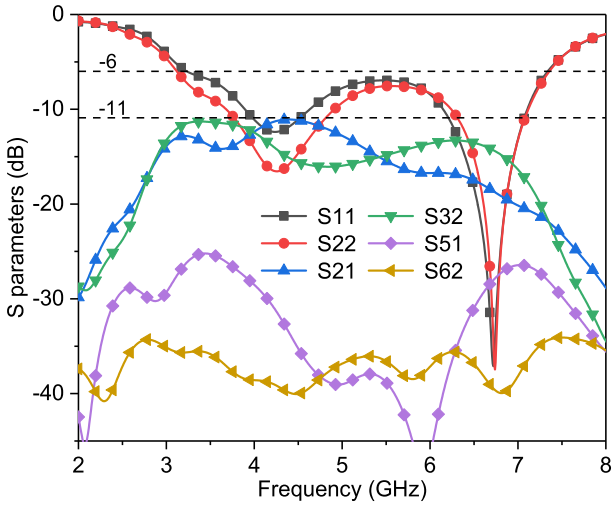

FIGURE 3. Simulated S parameters of the proposed antenna array.

of the antenna elements, only S parameters of Ant 1 and Ant 2 are given. From Fig. 3, it can be seen that two resonance modes are created, and the simulated reflection coefficients are less than −6 dB in the whole 3.3–7.1 GHz band. The isolation between two adjacent antenna elements in the array is better than 11 dB. The isolations between the other elements farther apart are much better, so they are not plotted in the figure.

III. DESIGN PROCESS AND METHODOLOGY

The design process of the antenna element is shown in Fig. 4. Besides, the reflection coefficients of the proposed antenna element (Ant 1) and two references (Ant 1A and Ant 1B) are shown in Fig. 5. The variations of the real and imaginary parts of the input impedance are shown in Fig. 6.

Ant 1A consists of an L-shaped aperture and a straight microstrip line on the front surface. The antenna excites two modes at the same time. As seen in Figs. 4 and 5, the low-frequency resonance at 4.95 GHz is generated by open-slot mode (M_{slot}, the length is about 13.9 mm) which is controlled by path CDE, while the high-frequency resonance at 9.34 GHz is generated by IFA mode (M_{IFA}, the length is about 10 mm) which is controlled by path FG [17]. Nevertheless, both modes have relatively high resonance frequencies, especially for IFA mode. Also, the matching of IFA mode needs to be improved.

For Ant 1B, a meandered line AA' is loaded at a distance of 3 mm from the tail of the feeding line. The width of gap BB' of the meandered line is fixed at 0.3 mm. As seen in Fig. 5, with the meandered line, the resonance frequencies of the two modes are moved to 4.22 GHz and 7.93 GHz, respectively, which are both lower than their original resonance frequencies. The matching of IFA mode also becomes better. The function of the narrow meandered portion AA' is a distributed inductor, whereas the function of the small gap BB' is a distributed capacitor. Therefore, when the meandered line is loaded into the feeding section, it can be considered

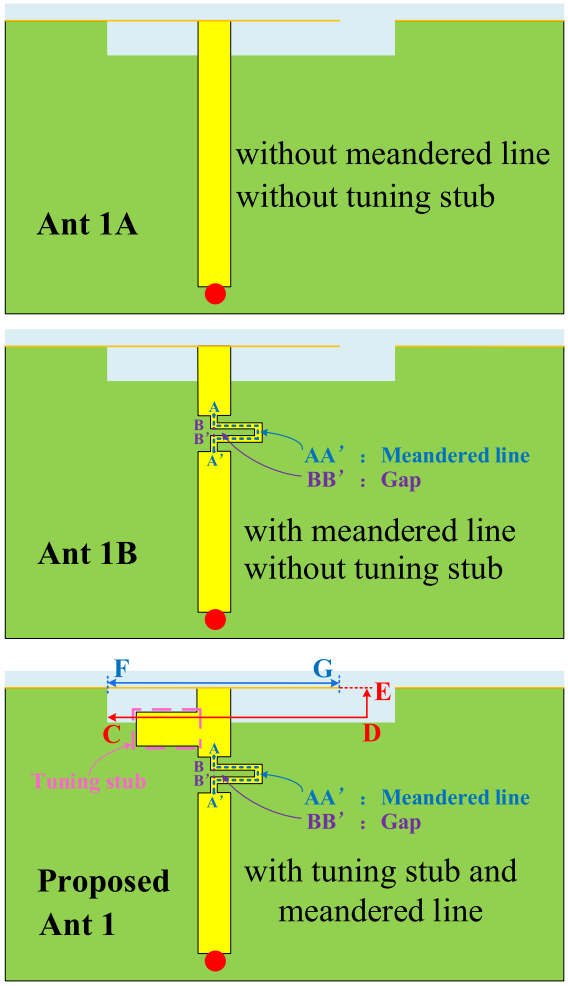

FIGURE 4. Evolution of the antenna element: Ant 1A (without meandered line and tuning stub), Ant 1B (with meandered line, without tuning stub), Proposed Ant 1 (with tuning stub and meandered line).

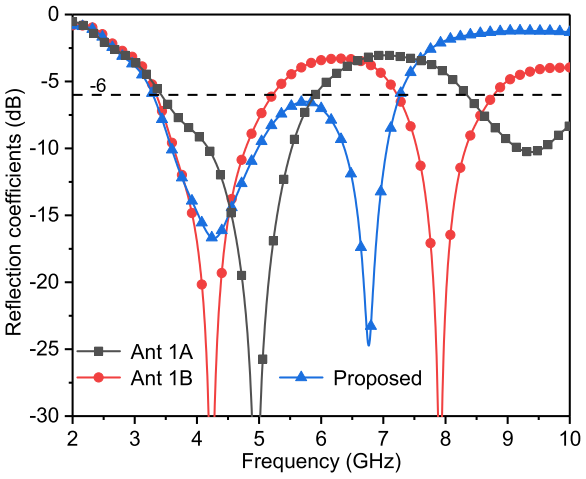

FIGURE 5. Simulated reflection coefficients of Ant 1A, Ant 1B, and proposed Ant 1.

as an impedance transformer which includes a composite LC network. Fig. 6 illustrates the evolution of the real and imaginary parts of the input impedance. It can be seen from

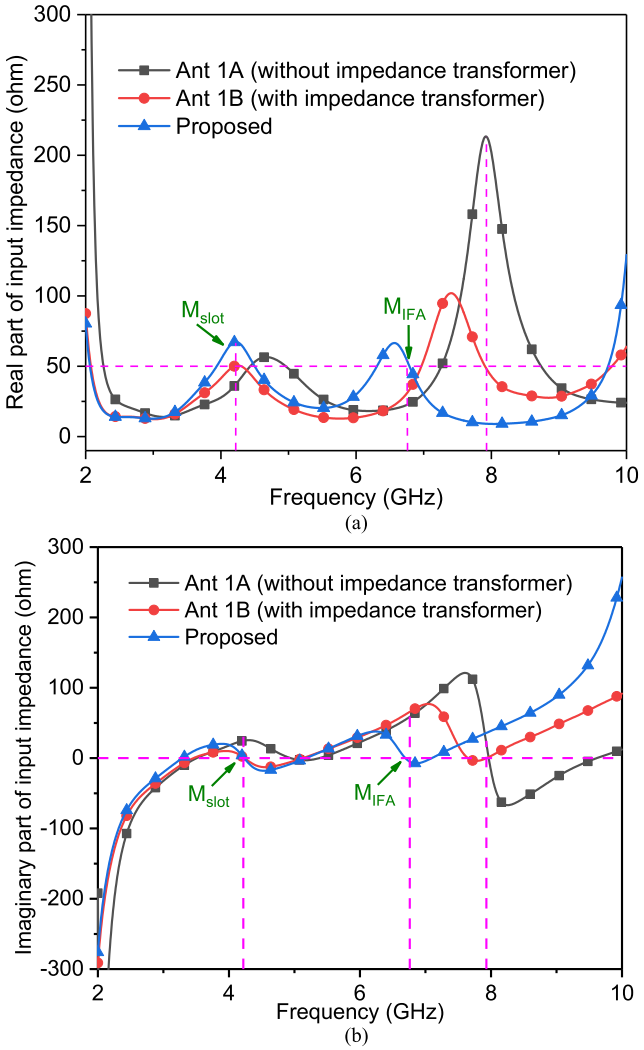

FIGURE 6. Simulated (a) Real part of input impedance and (b) Imaginary part of input impedance in the evolution process.

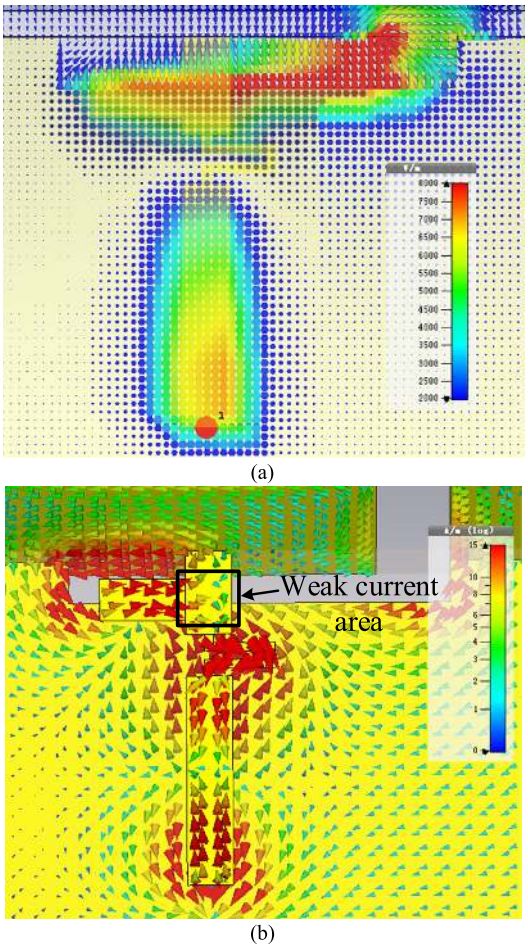

FIGURE 7. (a) Electric field distributions on the ground plane at 4.22 GHz (slot mode), (b) Surface current distributions at 6.76 GHz (IFA mode).

TABLE 1. Evolution of the proposed antenna element.

Name	Resonance Frequency (GHz)	Frequency Ratio
Ant 1A	4.95 and 9.34	1.89:1
Ant 1B	4.22 and 7.93	1.88:1
Proposed Ant 1	4.22 and 6.76	1.6:1

the Fig. 6(a) that the imaginary part curve near 4.22 GHz descends due to the compensation of the capacitive component of the impedance transformer. The resultant imaginary part hovers around zero, which is a good behavior for obtaining wideband feature. While at high frequency, as illustrated in Fig. 6(b), the impedance transformer functions more like a series LC circuit resonating at 7.93 GHz. The nature a series LC circuit is that across its resonance frequency, the impedance compensation effect changes from capacitive to inductive. Therefore, the imaginary part on the left side of 7.93 GHz decreases whereas that on the right side increases, which makes the impedance variation near this frequency tend to be smoother. And from Fig. 6(a), it is known that the real part at 7.93 GHz also varies from 210 ohm to approximately 50 ohm. Therefore, the IFA mode is shifted to 7.93 GHz. To sum up, the meandered impedance transformer mainly has two positive effects, i.e., (1) both two modes can be moved to lower frequency without increasing antenna size, and (2) the matching of IFA mode can be enhanced.

However, the working bandwidth of Ant 1B is still unable to completely cover 3.3–7.1 GHz, as the resonance frequency of IFA mode is still too high. Here, the best way to achieve a complete wideband coverage is to decrease the frequency ratio, which means tuning IFA mode to lower frequency while keeping the slot mode almost unchanged. Thus, a small tuning stub is added to the left side of the weak current area, which can be regarded as capacitive loading [see Fig. 7 (b)]. As shown in Table 1, the function of capacitive loading is that the resonance frequency ratio is reduced from 7.93 GHz: 4.22 GHz (1.88:1) to 6.76 GHz: 4.22 GHz (1.6:1) [18]. As depicted in Fig. 6(b), the imaginary part decreases remarkably near 6.76 GHz after adding the capacitive branch.

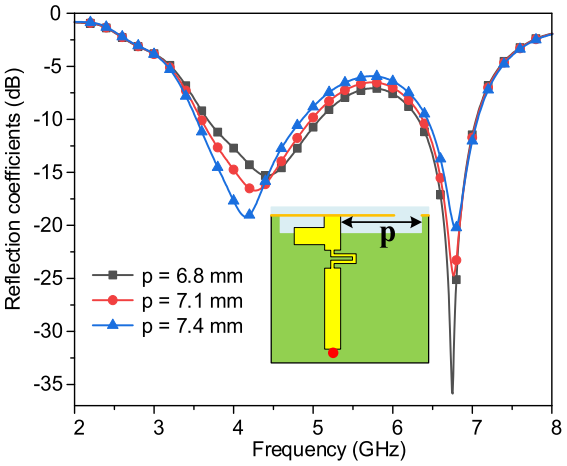

FIGURE 8. Simulated reflection coefficients as a function of parameter p: position of the feeding line.

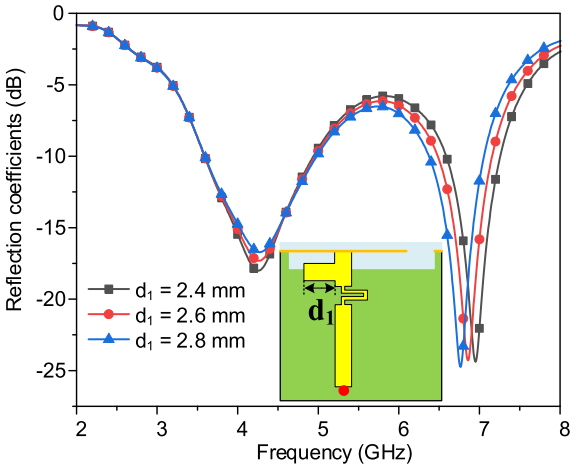

FIGURE 9. Simulated reflection coefficients as a function of parameter d_1: length of the tuning stub.

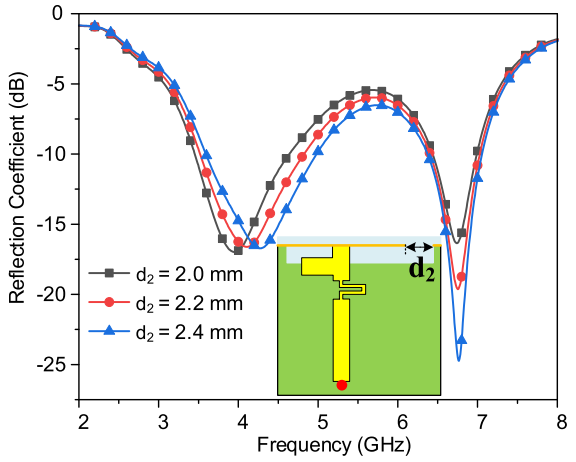

FIGURE 10. Simulated reflection coefficients as a function of parameter d_2: width of the slot etched on the metal rim.

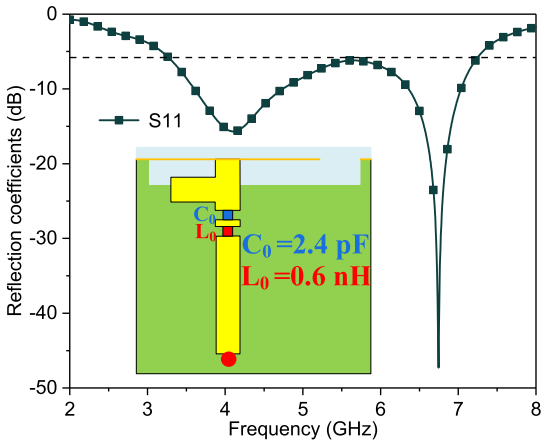

FIGURE 11. Simulated reflection coefficients of the antenna element with a series LC circuit.

Thus, a null of imaginary part is generated at 6.76 GHz. In addition, the tuning stub has very little coupling effect on the rectangular slot etched on the metal ground, so adding the tuning stub will only make the IFA mode move to the lower frequency, while keeping the slot mode still, thereby merging the two modes to achieve wideband coverage across 3.3–7.1 GHz.

Throughout the entire design procedure from Ant 1A to Ant 1, we can see that the three states of the evolution process are generally in accordance with the three steps of mode manipulation described in Section I, i.e., mode generation, mode adjustment, and mode combination. Firstly, for Ant 1A, diverse IFA and slot modes are created by a simple feeding line and an etched aperture. Secondly, for Ant 1B, to adjust the two modes, a meandered line acting as an impedance transformer is designed, leading to mode shifting and matching enhancement. Finally, for Ant 1, the two modes are combined to support the wide bandwidth, by introducing the capacitively loaded stub. The subtle mode manipulation is realized by two approaches, i.e., impedance matching and reactance loading, which jointly form the unique bandwidth enhancement methodology of this work.

Fig. 7(a) shows the electric field distribution on the ground plane at lower resonance frequency (4.22 GHz). It is seen that: (1) the direction of electric field is perpendicular to the slot path, and (2) the intensity of electric field gradually decreases from the open gap to the closed section (path CDE), which indicates that slot mode is excited. Fig. 7(b) shows the current distribution of the antenna metal portion at higher resonance frequency (6.76 GHz). As can be observed, the current mainly concentrates on the feeding line and the metal rim (path FG) enclosed by the etched aperture, which means that IFA mode is generated. The FG part on the metal frame is used as the radiating arm of IFA.

Several parametric studies are given in Figs. 8 to 10, to provide some design guidelines of the proposed antenna array. The impact of the position of feeding line (parameter p) is illustrated in Fig. 8. Due to the coupling effect of the feeding line on the slot, the slot mode is shifted to the lower band when the feeding line moves to the left. Meanwhile,

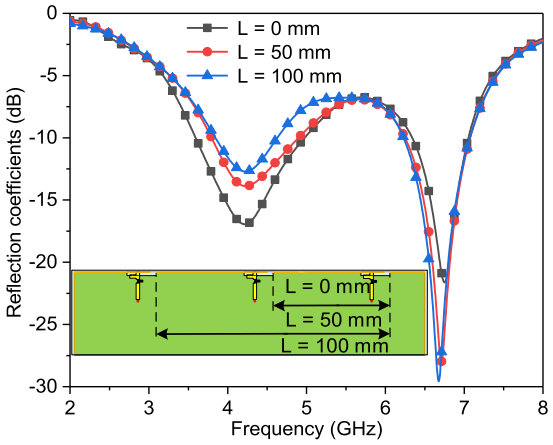

FIGURE 12. Simulated reflection coefficients when a single Ant 1 is moved along the long side edge.

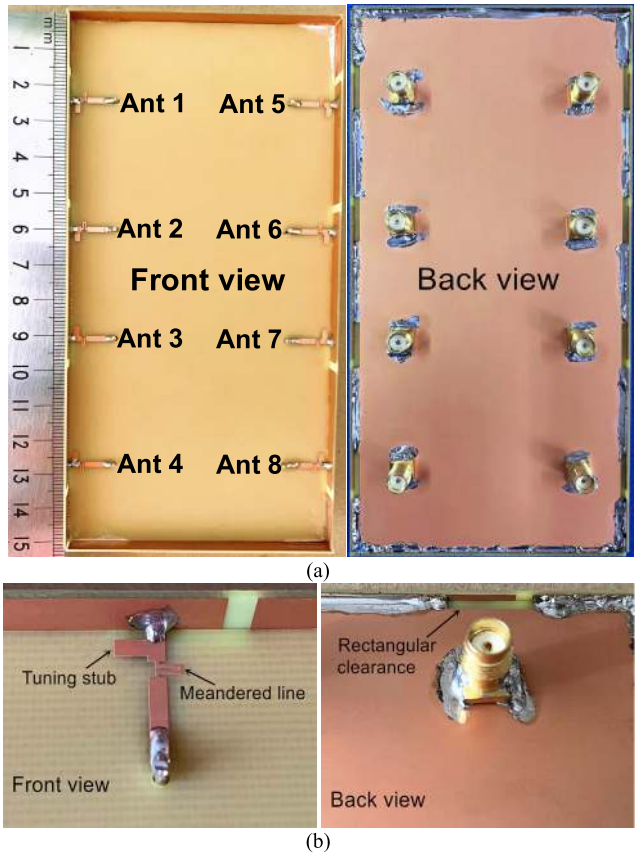

FIGURE 13. Photos of the fabricated MIMO antenna array: (a) front and back view of the antenna array, (b) front and back view of the antenna element.

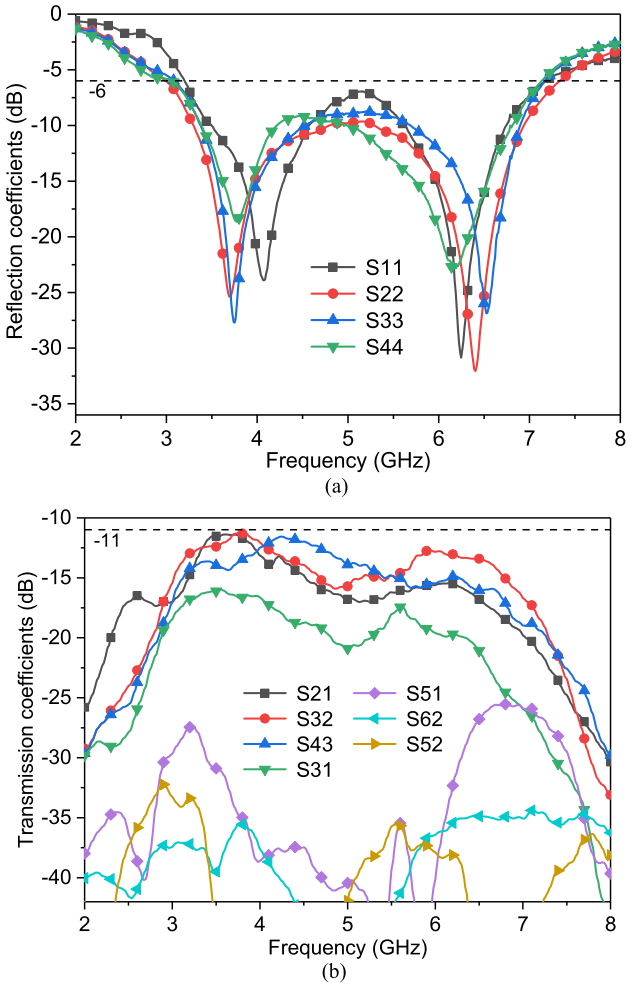

FIGURE 14. Measured (a) Reflection coefficients and (b) Transmission coefficients of the fabricated antenna array.

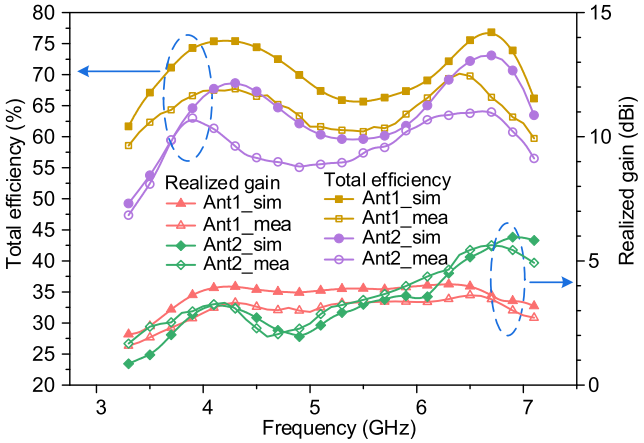

FIGURE 15. Total efficiency and realized gain of Ant 1 and Ant 2.

as the matching branch of IFA becomes shorter, the high-band matching becomes worse, which is in line with the basic theory of IFA mode. It can be seen from Fig. 9 that the length of the tuning stub (parameter d_1) affects capacitive loading. With the increase of d_1, the loaded capacitance is enhanced, so the IFA mode is moved towards lower frequency. At the same time, the slot mode almost stays still, which proves that capacitive loading has no strong effect on the slot mode. Fig. 10 reveals the effect of the width of the side-edge gap (parameter d_2). As can be observed, the variation of the gap mainly impacts the slot mode. A narrower opening leads to a lower resonance frequency, which is due to additional loaded capacitance.

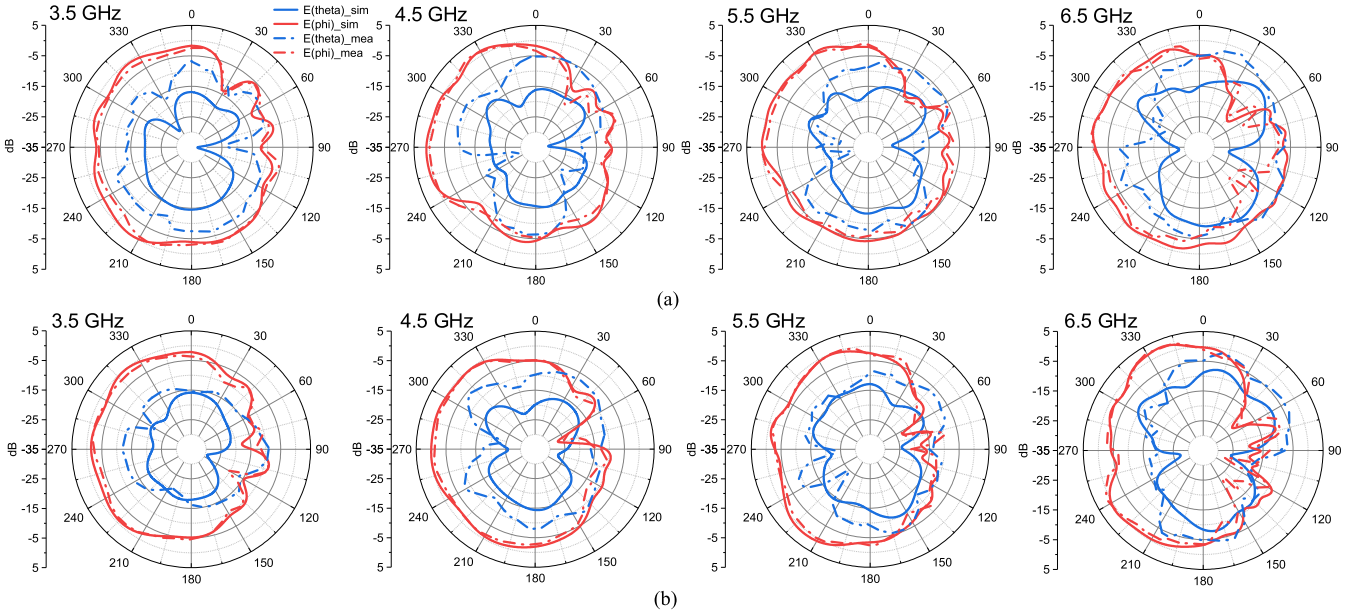

FIGURE 16. Simulated and measured radiation patterns in the xy plane for (a) Ant 1 and (b) Ant 2 working at 3.5 GHz, 4.5 GHz, 5.5 GHz, and 6.5 GHz.

As shown in Fig. 11, the antenna element can also cover 3.3–7.1 GHz when a series LC circuit ($C_0 = 2.4$ pF and $L_0 = 0.6$ nH) is used to replace the meandered line. However, chip capacitors and inductors will introduce additional insertion loss, so the design is not adopted for fabrication. Using the meandered line which can work as an impedance transformer, not only the antenna element can cover 3.3–7.1 GHz, but also no additional insertion loss is introduced.

Fig. 12 illustrates the change of reflection coefficient when the proposed antenna element moves along the long side edge. It is shown from the graph that when the antenna element moves from the right corner to the left corner (step = 50 mm), the lower-edge frequency of slot mode shifts slightly to the higher frequency. However, it can be expected that the antenna element can still cover the whole frequency band, by adjusting the position of the feeding line or changing the width of the side-edge gap.

IV. RESULTS AND CORRESPONDING DISCUSSION

A. S PARAMETERS

In order to verify the simulated results, a prototype of the proposed MIMO antenna array was fabricated. Fig. 13 shows the photographs of the antenna array on both sides. The enlarged pictures of the antenna element are also given. The S parameters were measured through Agilent E5071C Vector Network Analyzer. Fig. 14(a) demonstrates the reflection coefficients of Ants 1 to 4. It is clear that each antenna element can completely cover the bandwidth of 3.3–7.1 GHz, with reflection coefficients less than −6 dB. The transmission coefficients of some typical antenna pairs are shown in Fig. 14(b). The measured transmission coefficients between adjacent antenna elements (S21, S32 and S43) are better than 11 dB. Due to farther separation distance, the isolation between Ant 1 and Ant 3 (see S31) is higher than 17 dB. For other antenna elements arranged along opposite sides, the corresponding isolations (see S51, S62 and S52) are better than 25 dB. The measured and simulated results can well validate each other. In short, the measured results show that within 3.3–7.1 GHz, the proposed MIMO antenna array can meet the performance requirements of both bandwidth and isolation.

B. RADIATION PERFORMANCES

The simulated and measured results of total efficiency and realized gain are shown in Fig. 15. As can be seen from the graph, the simulated results of antenna efficiency range from 49%–76%. The measured efficiency decreases slightly, but it can still reach 47%–71%. The simulated realized gain of Ant 1 is 2 dBi–4 dBi, while that of Ant 2 is 0.9 dBi–6 dBi. The measured results are in good agreement with the simulation. The simulated and measured radiation patterns in the xy plane for Ant 1 and Ant 2 working at 3.5 GHz, 4.5 GHz, 5.5 GHz, and 6.5 GHz are shown in Fig. 16. Due to the symmetry of the array structure, the results of other elements are not given. The measured results of co-polarization are consistent with the simulated results. However, because of the interference level of the anechoic chamber, some deviations occur in the cross-polarization. As can be seen from the figure, both Ants 1 and 2 possess almost omnidirectional radiation. Across the entire wide operating bandwidth, their maximum radiations are directed outward (−y axis direction) from the long side edge, even though the main circuit board is surrounded by metal rims. For smartphone applications, this behavior is beneficial to signal reception. The simulated 3-D patterns of Ants 1 and 2 operating at 3.5 GHz, 4.5 GHz, 5.5 GHz and 6.5 GHz are shown in Fig. 17. It can be seen that the 3-D patterns are almost omnidirectional, and the

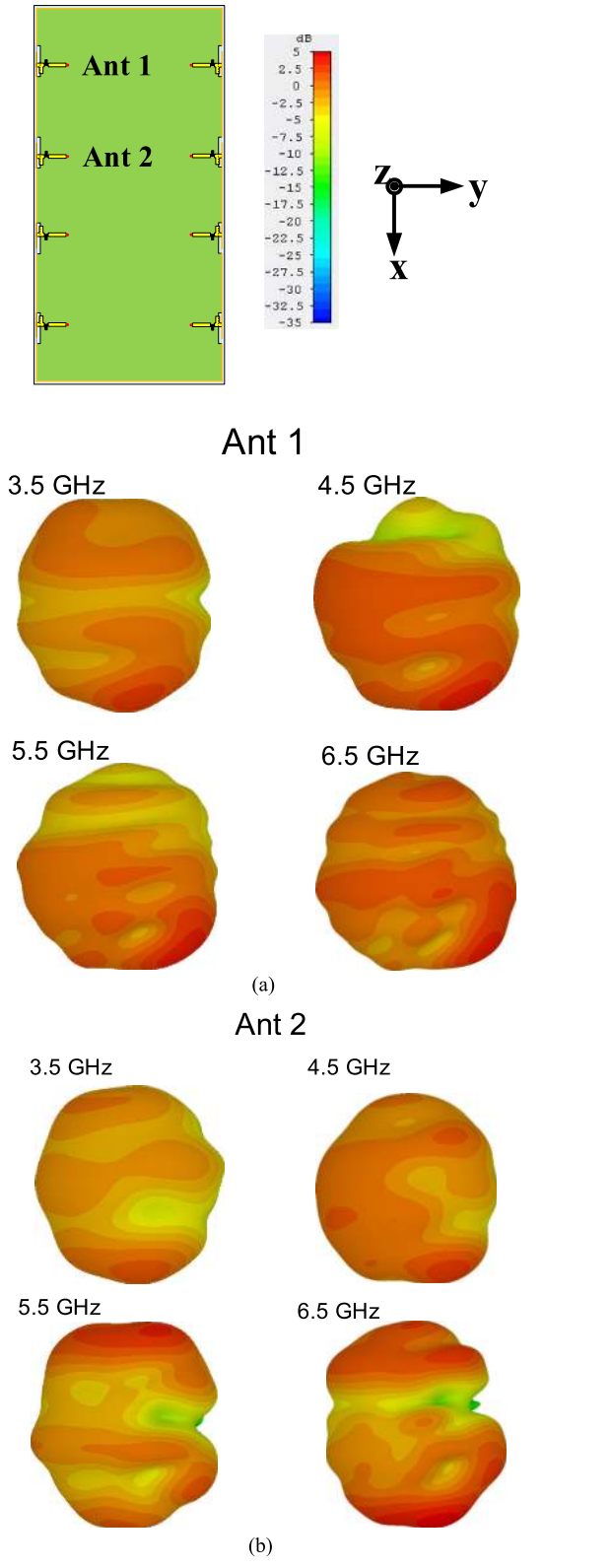

FIGURE 17. Simulated 3-D patterns for (a) Ant 1 and (b) Ant 2 working at 3.5 GHz, 4.5 GHz, 5.5 GHz, and 6.5 GHz.

maximum radiations are also directed away from the smartphone panel.

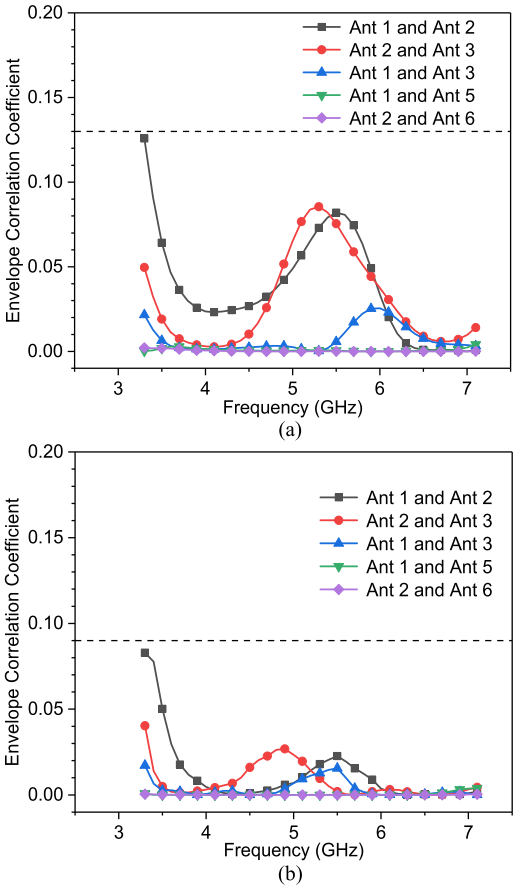

FIGURE 18. (a) Simulated and (b) measured ECCs of some typical antenna pairs.

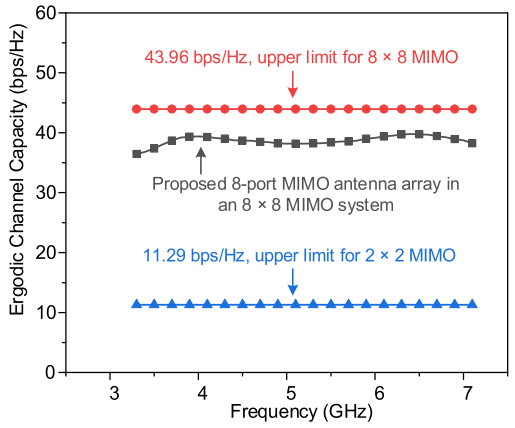

FIGURE 19. Calculated ergodic channel capacity of the proposed 8-port MIMO antenna array in an 8 × 8 MIMO antenna system.

C. MIMO PERFORMANCES

In order to evaluate the performances of the MIMO antenna array more comprehensively, the results of ECC and ergodic channel capacity are also given. The ECCs are calculated from the measured complex far field results of each antenna element in an isotropic channel that has 0-dB cross-polarization ratio [7], [19]. The simulated and

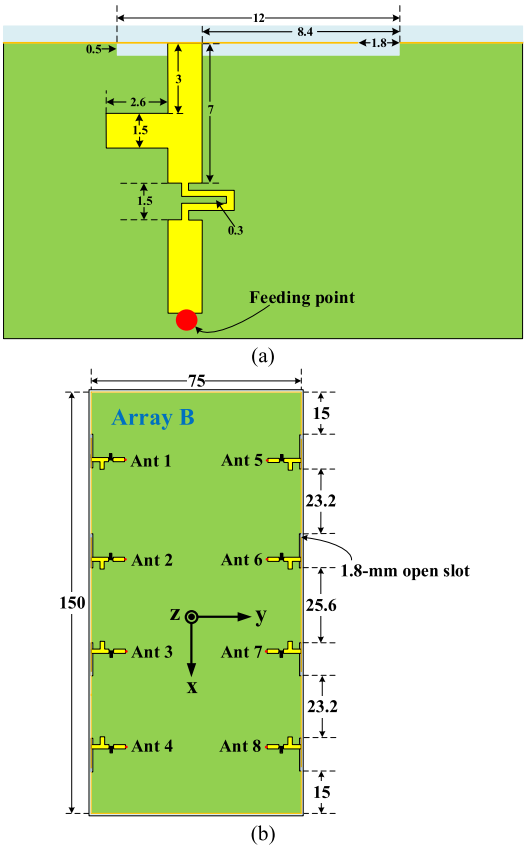

FIGURE 20. (a) Structure of the antenna element with smaller clearance size, (b) Structure of Array B.

calculated values of ECCs are demonstrated in Fig. 18. For Ant 1 and Ant 2, the simulated and calculated ECC values are less than 0.13 and 0.09, respectively. For Ant 2 and Ant 3, the simulated and calculated ECC values are less than 0.09 and 0.05, respectively. The ECC values between other antenna elements with longer distances (Ant 1 and Ant 3, Ant 1 and Ant 5, and Ant 2 and Ant 6) are close to 0. It is thus clear that the proposed MIMO antenna array has low correlation level, which makes it have favorable spatial diversity characteristics over the whole working frequencies.

The computed ergodic channel capacities are plotted in Fig. 19. Assuming that the propagation scenario satisfies independent and identically distributed Rayleigh fading, the Signal-to-Noise Ratio (SNR) at the receiver is 20 dB, and the transmitting antennas are ideal (uncorrelated and lossless), the ergodic channel capacities could be computed [20]. It can be seen that in the range of 3.3–7.1 GHz, the ergodic channel capacities of the proposed antenna array operating at 8 × 8 MIMO scheme are 36.45–39.78 bps/Hz, which is about 3.52 times higher than the upper limit (11.29 bps/Hz) of traditional 2 × 2 MIMO system in the same propagation environment. Therefore, the proposed 8-port MIMO antenna array also possesses strong spatial multiplexing capability.

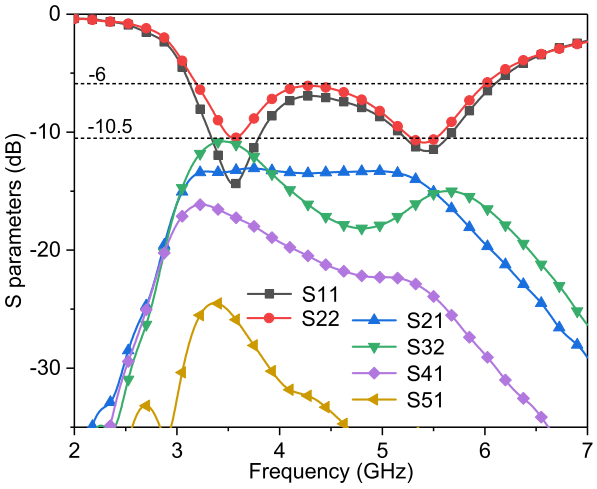

FIGURE 21. Simulated S parameters of Array B.

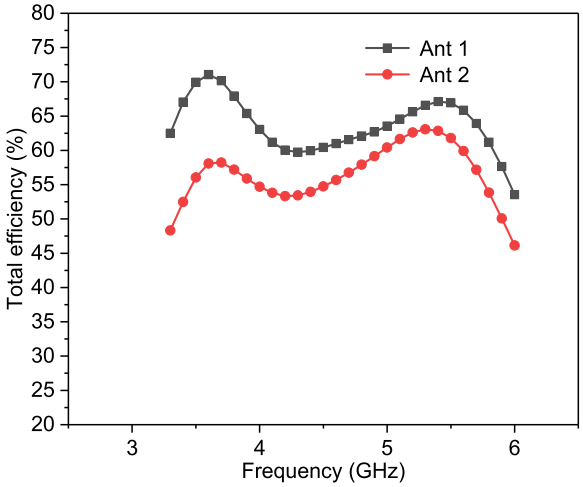

FIGURE 22. Simulated total efficiencies of Ant 1 and Ant 2 in Array B.

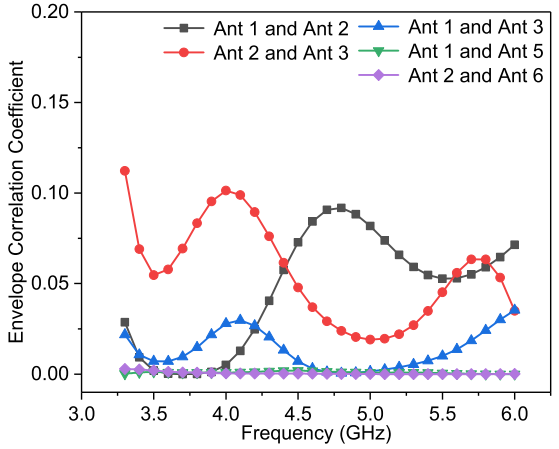

FIGURE 23. Simulated ECCs of some typical antenna pairs in Array B.

D. DESIGN WITH SMALLER CLEARANCE SIZE

In order to further reduce the clearance size, a modified design is proposed. The modified structure of the antenna

TABLE 2. A comprehensive comparison between the proposed work and other references.

Reference	Metal Rim	Effective Bandwidth (GHz)	Total Efficiency (%)^	Isolation (dB)^	ECC	Peak Channel Capacity (bps/Hz, 20-dB SNR)
Proposed	**With**	**3.3–4.2, 4.4–5, 5.15–7.1 (–6 dB)**	**47–70**	**> 11**	**< 0.09**	**39.8 (8×8)**
[3]	Without	3.4–3.6 (–10 dB), 5.15–5.925 (–6 dB)	50–68	> 12	< 0.1	39.7 (8×8)
[4]	Without	3.4–3.8, 5.15–5.925 (–6 dB)	41–82	> 12	< 0.15	37 (8×8) 29.5 (6×6)
[5]	With	2.496–2.69, 3.3–3.7 (–6 dB)	41–64	> 10.5	< 0.11	38.9 (8×8)
[6]	Without	1.49–1.56, 3.3–3.6, 4.8–5 (–6 dB)	51–78	> 10	< 0.23	Not given (8×8)
[7]	Without	3.4–3.8, 5.15–5.925 (–6 dB)	42–82	> 11	< 0.15	51.4 (10×10)
[8]	Without	3.4–3.6 (–10 dB)	Not given	> 11.7	< 0.1	Not given (8×8)
[20]	Without	3.4–3.6 (–6 dB)	40–60	> 10	< 0.25	38 (8×8)
[21]	With	3.4–3.6 (–6 dB)	45–60	> 12	< 0.1	37 (8×8)
[22]	With	2.496–2.69, 3.4–3.8 (–6 dB)	44–66	> 10.5	< 0.2	38.3 (8×8)
[23]	Without	3.4–3.6 (–6 dB)	55–59	> 10	Not given	16 (2×8)
[24]*	Without	3.4–3.6 (–10 dB)	62–78	> 10	< 0.2	40 (8×8)
[25]	Without	3.4–3.8 (–6 dB)	42–62	> 10	< 0.1	47 (10×10)
[26]	Without	2.55–2.65 (–10 dB)	48–63	> 12.5	< 0.15	40 (8×8)
[27]	Without	3.4–3.6 (–6 dB)	40–52	> 10	< 0.15	35 (8×8)
[28]	Without	3.4–3.8, 5.15–5.925 (–6 dB)	49–75	> 11	< 0.1	43.3 (8×10)
[29]	Without	3.4–3.6, 4.8–5 (–6 dB)	40–85	> 11.5	< 0.1	38.5 (8×8)
[30]	With	3.4–3.6 (–6 dB)	42–75	> 13	< 0.15	Not given (8×8)
[31]	Without	3.4–3.6 (–10 dB)	50–60	> 12.5	< 0.2	57 (12×12)
[32]	Without	3.4–3.6, 5.15–5.925 (–10 dB)	51–80	> 11.2	< 0.1	40.9 (8×8)
[33]	With	3.4–3.6 (–6 dB)	29.2–54.1	> 12.7	< 0.13	Not given (4×4)
[34]	Without	3.6–3.735 (–6 dB)	20–43	> 11.6	Not given	Not given (8×8)
[35]*	With	3.4–3.6 (–10 dB)	41–71	> 13	< 0.2	Not given (4×4)
[36]	Without	3.3–4.2 (–6 dB)	50–77	> 12	< 0.1	Not given (2×2)
[37]	Without	2.3–2.484, 2.496–2.69, 3.3–4.2, 4.4–5, 5.15–5.875 (–6 dB)	50–79	> 9	< 0.06	Not given (2×2)
[38]	Without	3.3–3.6 (–6 dB)	48–73	> 10	< 0.11	Not given (4×4)
[39]	Without	3.3–4.2, 4.4–5, 5.15–5.875 (–6 dB)	56–83	> 10	< 0.02	Not given (4×4)
[40]	Without	3.4–3.8 (–6 dB)	57–86	> 12	< 0.1	10.6 (2×2)
[41]	With	3.3–4.2, 4.4–5, 5.15–5.925 (–6 dB)	40–71	> 11	< 0.1	40 (8×8)
[42]	Without	2.496–2.69 (–6 dB)	46–60	> 13	< 0.1	39 (8×8)
[43]	Without	3.4–3.6, 5.725–5.875 (–6 dB)	48–80	> 10	< 0.15	42 (8×8)
[44]	Without	2.3–2.484, 3.3–3.8, 4.25–4.45 (–6 dB)	40–67	> 10	< 0.2	38.5 (8×8)
[45]	Without	3.4–3.6, 5.725–5.875 (–6 dB)	38–60	> 10	< 0.35	Not given (8×8)
[46]	Without	3.4–3.6, 5.725–5.875 (–6 dB)	41–59	> 10	< 0.2	63.8 (12×12)
[47]	Without	3.3–4.2, 4.8–5.0 (–6 dB)	53.8–79.1	> 11.5	< 0.12	40 (8×8)

* Only 5G antennas are considered for comparison.
^ Measured results.

element with an extremely narrow clearance is shown in Fig. 20(a). The clearance size of the new antenna element is only 12 mm × 0.5 mm (0.132 λ × 0.0055 λ at 3.3 GHz). Fig. 20(b) shows the eight-port MIMO antenna array composed of the new antenna elements, namely Array B. Although the clearance size of the antenna element is very small, it can be seen from Fig. 21 that the antenna element can still cover 3.3–6 GHz, and the isolations of some typical antenna pairs are greater than 10.5 dB. Fig. 22 illustrates that the simulated total efficiencies are higher than 46%, and Fig. 23 shows that the simulated ECC values are less than 0.12.

E. PERFORMANCE COMPARISON

A comprehensive comparison of the proposed work with previous works are listed in Table 2. Without loss of generality, more recent articles are added into this table [20]–[47]. It can be seen that most previous works fail to integrate metal rim, and none of the antenna arrays listed in the table can fully cover 3.3–7.1 GHz, which incorporates almost all licensed and unlicensed 5G bands for sub-7 GHz and NR-U. Although the MIMO antenna array in [37] can cover 2.3–6 GHz, its isolation and impedance matching are somewhat poor. In [39], the coupled feeding based MIMO antenna can cover 3.3–6 GHz, which lacks the 5.9–7.1 GHz band for NR-U. The common weakness of [37] and [39] is that neither of them is compatible with the metal rim environment that has become the mainstream of modern terminal devices. In [41], an 8-antenna array covering 3.3–6 GHz for metal-rimmed mobile phones is introduced, but it also fails to cover the additional unlicensed 5.9–7.1 GHz band. Besides, its ground clearance size (15 mm × 3 mm) is much larger than the

TABLE 3. Clearance size comparison.

Reference	Effective Bandwidth (GHz)	Clearance Size (mm × mm)/(mm^2)
Proposed	**3.3–4.2, 4.4–5, 5.15–7.1 (–6 dB)**	**12.4 ×1.5/18.6**
Array B	**3.3–4.2, 4.4–5, 5.15–5.925 (–6 dB)**	**12 ×0.5/6**
[5]	2.496–2.69, 3.3–3.7 (–6 dB)	9.8 × 3/29.4
[21]	3.4–3.6 (–6 dB)	9 × 1/9
[22]	2.496–2.69, 3.4–3.8 (–6 dB)	21 × 3/63
[30]	3.4–3.6 (–6 dB)	10.8 × 1/10.8 (open slot) 28.8 × 1/28.8 (closed slot)
[33]^	3.4–3.6 (–6 dB)	25 × 1.5/37.5
[35]	3.4–3.6 (–10 dB)	32 × 2/64
[41]	3.3–4.2, 4.4–5, 5.15–5.925 (–6 dB)	15 × 3/45

^ Design using antenna pairs.

TABLE 4. Comparison of wideband performance.

Reference	Effective Bandwidth (GHz)	Metal Rim	Number of Modes
Proposed	**3.3–4.2, 4.4–5, 5.15–7.1 (–6 dB)**	**With**	**2**
Array B	**3.3–4.2, 4.4–5, 5.15–5.925 (–6 dB)**	**With**	**2**
[3]	3.4–3.6 (–10 dB), 5.15–5.925 (–6 dB)	Without	2
[4]	3.4–3.8, 5.15–5.925 (–6 dB)	Without	2
[5]	2.496–2.69, 3.3–3.7 (–6 dB)	With	2
[6]	1.49–1.56, 3.3–3.6, 4.8–5 (–6 dB)	Without	3
[7]	3.4–3.8, 5.15–5.925 (–6 dB)	Without	2
[11]	3.3–4.2, 4.4–5 (–10 dB)	Without	3
[22]	2.496–2.69, 3.4–3.8 (–6 dB)	With	2
[28]	3.4–3.8, 5.15–5.925 (–6 dB)	Without	2
[29]	3.4–3.6, 4.8–5 (–6 dB)	Without	2
[32]	3.4–3.6, 5.15–5.925 (–10 dB)	Without	2
[37]	2.3–2.484, 2.496–2.69, 3.3–4.2, 4.4–5, 5.15–5.875 (–6 dB)	Without	3
[39]	3.3–4.2, 4.4–5, 5.15–5.875 (–6 dB)	Without	3
[41]	3.3–4.2, 4.4–5, 5.15–5.925 (–6 dB)	With	2
[43]	3.4–3.6, 5.725–5.875 (–6 dB)	Without	2
[44]	2.3–2.484, 3.3–3.8, 4.25–4.45 (–6 dB)	Without	2/3
[45]	3.4–3.6, 5.725–5.875 (–6 dB)	Without	2
[46]	3.4–3.6, 5.725–5.875 (–6 dB)	Without	2
[47]	3.3–4.2, 4.8–5.0 (–6 dB)	Without	2

proposed work (12.4 mm × 1.5 mm). Apart from wider bandwidth, compared with some 8-antenna arrays, the peak channel capacity of the proposed antenna array is higher than the works reported in [3]–[5], [20]–[22], [27], [29], [42], [44]. In addition, the ECC of the proposed antenna array is also relatively low.

Besides, Table 3 and Table 4 further illustrate the highlights of the proposed work. Table 3 shows the comparison of

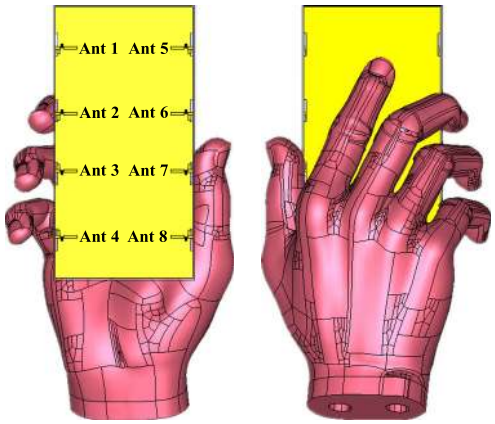

FIGURE 24. Typical case of holding a smartphone in one hand.

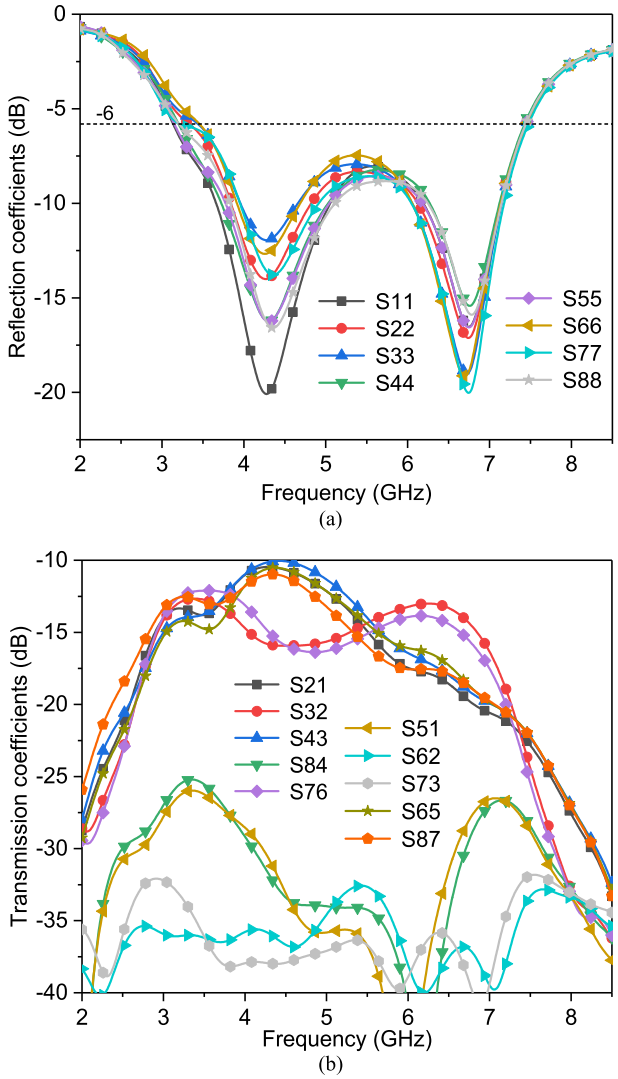

FIGURE 25. Simulated (a) reflection coefficients, (b) transmission coefficients of the proposed antenna array while holding a smartphone in one hand.

proposed antenna with others working in the metal-rimmed platform. Here, the antennas with printed metal patterns on the side-edge plastic frames are not considered, which is due

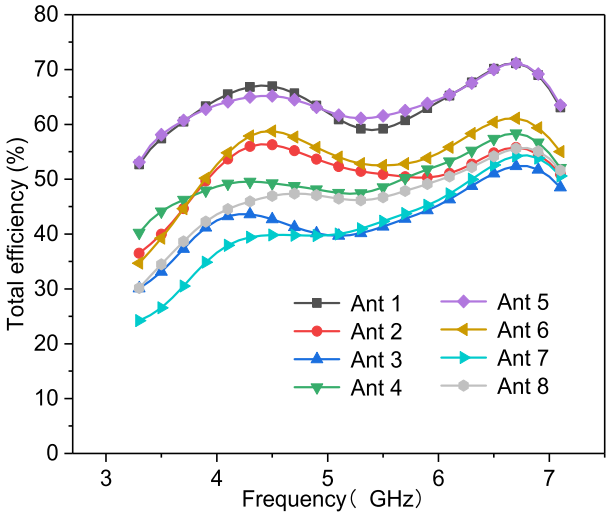

FIGURE 26. Simulated total efficiency of the proposed antenna array while holding a smartphone in one hand.

to the different design concepts and working environments (such designs usually do not require clearance, as the radiators adhere to the frames). It is clear from Table 3 that this design uses lesser clearance but achieves the widest bandwidth. In addition, for Array B, the clearance size of the antenna element is only 12 mm × 0.5 mm. Compared with other references in Table 3, the clearance size of Array B is the smallest, but it can still cover a very wide bandwidth of 3.3–6 GHz. Meanwhile, Table 4 compares the two arrays (proposed and Array B) with those multiband 5G MIMO handset antennas in terms of number of modes and metal rim integration. As can be seen, only a few antennas are integrated with metal rims. Besides, the proposed work achieves the widest bandwidth (3.3–7.1 GHz) by using two diverse modes. Similarly, Array B covers a consecutive 3.3–6 GHz band also by utilizing only two modes. Nevertheless, in contrast, the other works with two or even three modes generated have shown narrower bandwidths.

Thus, it can be seen that the advantages of the proposed MIMO antenna are mainly embodied in its wide bandwidth, small size, no lumped elements, simple structure, easy processing, and metal-rim integration. The proposed MIMO antenna provides a good application-oriented design, which realizes wideband effect that the previous works failed to achieve in such a simple way. However, because this design mainly focuses on wideband design, although the isolation between antenna elements can reach 11 dB, there is no additional decoupling design. Several works with novel decoupling techniques are expected to be promising for further improving the isolation of the proposed work [48]–[56].

F. EFFECTS OF USERS' HAND

Fig. 24 shows a typical case of a user holding a mobile phone in one hand. Fig. 25 illustrates the S parameters of each antenna element in this case. From Fig. 25(a), it can be seen that the effective frequency bands of Ants 2, 3, and 6 are slightly shifted to higher frequency, but they can be moved by adjusting the width of the side-edge gap. Fig. 25(b) demonstrates the isolations with user's hand. It can be seen from the figure that the isolations of typical antenna pairs are greater than 10 dB when the mobile phone is touched. Fig. 26 shows the total efficiencies of the antenna elements. Although the total efficiencies decrease in varying degrees, the lowest efficiency can still reach 24%, which reveals the application potential of the proposed MIMO antenna array in the actual 5G mobile communication.

V. CONCLUSION

A wideband 8-antenna MIMO array which can completely cover 3.3–7.1 GHz for future 5G metal-rimmed smartphones is presented in this paper. The proposed design realizes wideband coverage simply by means of mode manipulation, in which IFA and slot modes are generated, adjusted and combined. The methods of impedance matching and capacitive loading are employed in the design process, to achieve frequency adjustment, mode combination, and antenna miniaturization. The proposed antenna array has good performances in the whole frequency range, with isolation >11 dB, total efficiency > 47%, ECC < 0.09 and the ergodic channel capacity reaching 39.78 bps/Hz. With the advent of 5G communication, the proposed antenna array can be a good candidate for next-generation terminal devices.

REFERENCES

[1] Qualcomm. *Making 5G NR a Commercial Reality*. Accessed: Mar. 2019. [Online]. Available: https://www.qualcomm.com/media/documents/files/making-5g-nr-a-commercial-reality.pdf
[2] *Technical Specification 38.101-1: NR; User Equipment (UE) Radio Transmission and Reception; Part 1: Range 1 Standalone*. Accessed: Jun. 2019.[Online]. Available: https://portal.3gpp.org/desktopmodules/Specifications/SpecificationDetails.aspx?specificationId=3283
[3] H. Zou, Y. Li, C.-Y.-D. Sim, and G. Yang, "Design of 8×8 dual-band MIMO antenna array for 5G smartphone applications," *Int. J. RF Microw. Comput. Aided Eng.*, vol. 28, no. 9, Nov. 2018, Art. no. e21420.
[4] Y. Li, C.-Y.-D. Sim, Y. Luo, and G. Yang, "12-Port 5G massive MIMO antenna array in Sub-6GHz mobile handset for LTE bands 42/43/46 applications," *IEEE Access*, vol. 6, pp. 344–354, 2017.
[5] H. Zou, Y. Li, B. Xu, Y. Luo, M. Wang, and G. Yang, "A dual-band eight-antenna multi-input multi-output array for 5G metal-framed smartphones," *Int. J. RF Microw. Comput. Aided Eng.*, vol. 29, no. 7, Jul. 2019, Art. no. e21745.
[6] C. Huang, Y.-C. Jiao, and Z.-B. Weng, "Novel compact CRLH-TL-based tri-band MIMO antenna element for the 5G mobile handsets," *Microw. Opt. Technol. Lett.*, vol. 60, no. 10, pp. 2559–2564, Oct. 2018.
[7] Y. Li, C.-Y.-D. Sim, Y. Luo, and G. Yang, "Multiband 10-antenna array for sub-6 GHz MIMO applications in 5-G smartphones," *IEEE Access*, vol. 6, pp. 28041–28053, 2018.
[8] H. Shi, X. Zhang, J. Li, P. Jia, J. Chen, and A. Zhang, "3.6-GHz eight-antenna MIMO array for mobile terminal applications," *AEU Int. J. Electron. Commun.*, vol. 95, pp. 342–348, Oct. 2018.
[9] I. R. R. Barani and K.-L. Wong, "Dual-feed U-slot antenna having low envelope correlation coefficients for the LTE MIMO operation in the metal-framed smartphone," *Microw. Opt. Technol. Lett.*, vol. 60, no. 2, pp. 295–302, Feb. 2018.
[10] I. R. R. Barani and K.-L. Wong, "Integrated inverted-f and open-slot antennas in the metal-framed smartphone for 2×2 LTE LB and 4×4 LTE M/HB MIMO Operations," *IEEE Trans. Antennas Propag.*, vol. 66, no. 10, pp. 5004–5012, Oct. 2018.
[11] A. Zhao and Z. Ren, "Wideband MIMO antenna systems based on coupled-loop antenna for 5G N77/N78/N79 applications in mobile terminals," *IEEE Access*, vol. 7, pp. 93761–93771, 2019.

[12] H. Xu, H. Wang, S. Gao, H. Zhou, Y. Huang, Q. Xu, and Y. Cheng, "A compact and low-profile loop antenna with six resonant modes for LTE smartphone," *IEEE Trans. Antennas Propag.*, vol. 64, no. 9, pp. 3743–3751, Sep. 2016.

[13] *Technical Report 37.890: Feasibility Study on 6 GHz for LTE and NR in Licensed and Unlicensed Operations*. Accessed: Jun. 2019. [Online]. Available: https://portal.3gpp.org/desktopmodules/Specifications/SpecificationDetails.aspx?specificationId=3436

[14] *Technical Report 38.889: Study on NR-Based Access to Unlicensed Spectrum*. Accessed: Jun. 2019. [Online]. Available: https://portal.3gpp.org/desktopmodules/Specifications/SpecificationDetails.aspx?specificationId=3235

[15] H. Wang, D. Zhou, L. Xue, S. Gao, and H. Xu, "Modal analysis and excitation of wideband slot antennas," *IET Microw. Antennas Propag.*, vol. 11, no. 13, pp. 1887–1891, Oct. 2017.

[16] M. Zheng, H. Y. Wang, and Y. Hao, "Internal hexa-band folded monopole/dipole/loop antenna with four resonances for mobile device," *IEEE Trans. Antennas Propag.*, vol. 60, no. 6, pp. 2880–2885, Jun. 2012.

[17] M. Stanley, Y. Huang, H. Wang, H. Zhou, Z. Tian, and Q. Xu, "A novel reconfigurable metal rim integrated open slot antenna for octa-band smartphone applications," *IEEE Trans. Antennas Propag.*, vol. 65, no. 7, pp. 3352–3363, Jul. 2017.

[18] H. Wang and M. Zheng, "Triple-band wireless local area network monopole antenna," *IET Microwaves, Antennas Propag.*, vol. 2, no. 4, pp. 367–372, Jun. 2008.

[19] J. Y. Deng, J. Li, L. Zhao, and L. Guo, "A dual-band inverted-F MIMO antenna with enhanced isolation for WLAN applications," *IEEE Antennas Wireless Propag. Lett.*, vol. 16, pp. 2270–2273, Jun. 2017.

[20] K.-L. Wong, J.-Y. Lu, L.-Y. Chen, W.-Y. Li, and Y.-L. Ban, "8-antenna and 16-antenna arrays using the quad-antenna linear array as a building block for the 3.5-GHz LTE MIMO operation in the smartphone," *Microw. Opt. Technol. Lett.*, vol. 58, no. 1, pp. 174–181, Jan. 2016.

[21] J.-Y. Lu, K.-L. Wong, and W.-Y. Li, "Compact eight-antenna array in the smartphone for the 3.5-GHz LTE 8 × 8 MIMO operation," in *Proc. IEEE 5th Asia–Pacific Conf. Antennas Propag. (APCAP)*, Kaohsiung, Taiwan, Jul. 2016, pp. 323–324.

[22] Y. Li, C.-Y.-D. Sim, Y. Luo, and G. Yang, "Metal-frame-integrated eight-element multiple-input multiple-output antenna array in the long term evolution bands 41/42/43 for fifth generation smartphones," *Int. J. RF Microw. Comput. Aided Eng.*, vol. 29, no. 1, Jan. 2019, Art. no. e21495.

[23] A. A. Al-Hadi, J. Ilvonen, R. Valkonen, and V. Viikari, "Eight-element antenna array for diversity and MIMO mobile terminal in LTE 3500 MHz band," *Microw. Opt. Technol. Lett.*, vol. 56, no. 6, pp. 1323–1327, Jun. 2014.

[24] Y.-L. Ban, C. Li, C.-Y.-D. Sim, G. Wu, and K.-L. Wong, "4G/5G multiple antennas for future multi-mode smartphone applications," *IEEE Access*, vol. 4, pp. 2981–2988, 2016.

[25] K.-L. Wong and J. Y. Lu, "3.6-GHz 10-antenna array for mimo operation in the smartphone," *Microw. Opt. Technol. Lett.*, vol. 57, no. 7, pp. 1699–1704, Jul. 2015.

[26] M.-Y. Li, Y.-L. Ban, Z.-Q. Xu, G. Wu, C.-Y.-D. Sim, K. Kang, and Z.-F. Yu, "Eight-port orthogonally dual-polarized antenna array for 5G smartphone applications," *IEEE Trans. Antennas Propag.*, vol. 64, no. 9, pp. 3820–3830, Sep. 2016.

[27] K.-L. Wong, C.-Y. Tsai, and J.-Y. Lu, "Two asymmetrically mirrored gap-coupled loop antennas as a compact building block for eight-antenna MIMO array in the future smartphone," *IEEE Trans. Antennas Propag.*, vol. 65, no. 4, pp. 1765–1778, Apr. 2017.

[28] Y. Li and G. Yang, "Dual-mode and triple-band 10-antenna handset array and its multiple-input multiple-output performance evaluation in 5G," *Int. J. RF Microw. Comput. Aided Eng.*, vol. 29, no. 2, Feb. 2019, Art. no. e21538.

[29] J. L. Guo, L. Cui, C. Li, and B. H. Sun, "Side-edge frame printed eight-port dual-band antenna array for 5G smartphone applications," *IEEE Trans. Antennas Propag.*, vol. 66, no. 12, pp. 7412–7417, Dec. 2018.

[30] D. Huang, Z. Du, and Y. Wang, "Slot antenna array for fifth generation metal frame mobile phone applications," *Int. J. RF Microw. Comput. Aided Eng.*, vol. 29, no. 9, Sep. 2019, Art. no. e21841.

[31] M.-Y. Li, Y.-L. Ban, Z.-Q. Xu, J. Guo, and Z.-F. Yu, "Tri-polarized 12-antenna MIMO array for future 5G smartphone applications," *IEEE Access*, vol. 6, pp. 6160–6170, 2017.

[32] J. Li, X. Zhang, Z. Wang, X. Chen, J. Chen, Y. Li, and A. Zhang, "Dual-band eight-antenna array design for MIMO applications in 5G mobile terminals," *IEEE Access*, vol. 7, pp. 71636–71644, 2019.

[33] L. Chang, Y. Yu, K. Wei, and H. Wang, "Polarization-orthogonal co-frequency dual antenna pair suitable for 5G MIMO smartphone with metallic bezels," *IEEE Trans. Antennas Propag.*, vol. 67, no. 8, pp. 5212–5220, Aug. 2019.

[34] C. Deng, D. Liu, and X. Lv, "Tightly-arranged four-element MIMO antennas for 5G mobile terminals," *IEEE Trans. Antennas Propag.*, to be published. doi: 10.1109/TAP.2019.2922757.

[35] Q. Chen, H. Lin, J. Wang, L. Ge, Y. Li, T. Pei, and C.-Y. D. Sim, "Single ring slot-based antennas for metal-rimmed 4G/5G smartphones," *IEEE Trans. Antennas Propag.*, vol. 67, no. 3, pp. 1476–1487, Mar. 2019.

[36] K.-L. Wong, B.-W. Lin, and S.-E. Lin, "High-isolation conjoined loop multi-input multi-output antennas for the fifth-generation tablet device," *Microw. Opt. Technol. Lett.*, vol. 61, no. 1, pp. 111–119, Jan. 2019.

[37] K.-L. Wong, Y.-H. Chen, and W.-Y. Li, "Conjoined ultra-wideband (2,300-6,000 MHz) dual antennas for LTE HB/WiFi/5G multi-input multi-output operation in the fifth-generation tablet device," *Microw. Opt. Technol. Lett.*, vol. 61, no. 8, pp. 1958–1963, Aug. 2019.

[38] L. Sun, H. Feng, Y. Li, and Z. Zhang, "Tightly arranged orthogonal mode antenna for 5G MIMO mobile terminal," *Microw. Opt. Technol. Lett.*, vol. 60, no. 7, pp. 1751–1756, Jul. 2018.

[39] K.-L. Wong, Y.-H. Chen, and W.-Y. Li, "Decoupled compact ultra-wideband MIMO antennas covering 3300~6000 MHz for the fifth-generation mobile and 5GHz-WLAN operations in the future smartphone," *Microw. Opt. Technol. Lett.*, vol. 60, no. 10, pp. 2345–2351, Oct. 2018.

[40] K.-L. Wong and H.-J. Chang, "Hybrid dual-antenna for the 3.6-GHz LTE operation in the tablet computer," *Microw. Opt. Technol. Lett.*, vol. 57, pp. 2592–2598, Nov. 2015.

[41] X. Zhang, Y. Li, W. Wang, and W. Shen, "Ultra-wideband 8-port MIMO antenna array for 5G metal-frame smartphones," *IEEE Access*, vol. 7, pp. 72273–72282, 2019.

[42] M.-Y. Li, Z.-Q. Xu, Y.-L. Ban, C.-Y.-D. Sim, and Z.-F. Yu, "Eight-port orthogonally dual-polarised MIMO antennas using loop structures for 5G smartphone," *IET Microw. Antennas Propag.*, vol. 11, no. 12, pp. 1810–1816, Sep. 2017.

[43] K.-L. Wong, B.-W. Lin, and B. W.-Y. Li, "Dual-band dual inverted-F/loop antennas as a compact decoupled building block for forming eight 3.5/5.8-GHz MIMO antennas in the future smartphone," *Microw. Opt. Technol. Lett.*, vol. 59, no. 11, pp. 2715–2721, Nov. 2017.

[44] X. Shi, M. Zhang, H. Wen, and J. Wang, "Compact quadruple band MIMO antenna for 5G mobile applications," in *Proc. 12th Eur. Conf. Antennas Propag. (EUCAP)*, London, UK, Apr. 2018, pp. 1–5.

[45] W.-Y. Li, W. Chung, and K.-L. Wong, "Compact quad-offset Loop/IFA hybrid antenna array for forming eight 3.5/5.8 GHz MIMO antennas in the future smartphone," in *Proc. Int. Symp. Antennas Propag. (ISAP)*, Busan, Korea (South), Oct. 2018, pp. 1–2.

[46] Z. Tian, R. Chen, and C. Li, "Dual-band inverted F-shaped antenna array for sub-6 GHz smartphones," in *Proc. IEEE 89th Veh. Technol. Conf.*, Kuala Lumpur, Malaysia, Apr./May 2019, pp. 1–5.

[47] L. Cui, J. Guo, Y. Liu, and C.-Y.-D. Sim, "An 8-element dual-band MIMO antenna with decoupling stub for 5G smartphone applications," *IEEE Antennas Wireless Propag. Lett.*, to be published. doi: 10.1109/LAWP.2019.2937851.

[48] J. Ouyang, F. Yang, and Z. M. Wang, "Reducing mutual coupling of closely spaced microstrip MIMO antennas for WLAN application," *IEEE Antennas Wireless Propag. Lett.*, vol. 10, pp. 310–313, 2011.

[49] A. Yu and X. Zhang, "A novel method to improve the performance of microstrip antenna arrays using a dumbbell EBG structure," *IEEE Antennas Wireless Propag. Lett.*, vol. 2, no. 1, pp. 170–172, 2003.

[50] H. S. Farahani, M. Veysi, M. Kamyab, and A. Tadjalli, "Mutual coupling reduction in patch antenna arrays using a UC-EBG superstrate," *IEEE Antennas Wireless Propag. Lett.*, vol. 9, pp. 57–59, 2010.

[51] M. M. B. Suwailam, O. F. Siddiqui, and O. M. Ramahi, "Mutual coupling reduction between microstrip patch antennas using slotted-complementary split-ring resonators," *IEEE Antennas Wireless Propag. Lett.*, vol. 9, pp. 876–878, 2010.

[52] X. M. Yang, X. G. Liu, X. Y. Zhou, and T. J. Cui, "Reduction of mutual coupling between closely packed patch antennas using waveguided metamaterials," *IEEE Antennas Wireless Propag. Lett.*, vol. 11, pp. 389–391, 2012.

[53] S. Farsi, H. Aliakbarian, D. Schreurs, B. Nauwelaers, and G. A. E. Vandenbosch, "Mutual coupling reduction between planar antennas by using a simple microstrip U-section," *IEEE Antennas Wireless Propag. Lett.*, vol. 11, pp. 1501–1503, 2012.

[54] M. G. Alsath, M. Kanagasabai, and B. Balasubramanian, "Implementation of slotted meander-line resonators for isolation enhancement in microstrip patch antenna arrays," *IEEE Antennas Wireless Propag. Lett.*, vol. 12, pp. 15–18, 2013.
[55] X. Yang, Y. Liu, Y.-X. Xu, and S.-X. Gong, "Isolation enhancement in patch antenna array with fractal UC-EBG structure and cross slot," *IEEE Antennas Wireless Propag. Lett.*, vol. 16, pp. 2175–2178, 2017.
[56] L. Zhao, F. Liu, X. Shen, G. Jing, Y.-M. Cai, and Y. Li, "A high-pass antenna interference cancellation chip for mutual coupling reduction of antennas in contiguous frequency bands," *IEEE Access*, vol. 6, pp. 38097–38105, 2018.

QINYI CAI was born in Shanghai, China, in 1995. She received the B.S. degree from Shanghai University, Shanghai, China, in 2018, where she is currently pursuing the M.S. degree in electromagnetic field and microwave technology with the School of Communication and Information Engineering.

Her current research interests include electrically small antennas, MIMO antennas, and microstrip antennas.

YIXIN LI was born in Hunan, China, in 1994. He received the B.S. and M.S. degrees from Shanghai University, Shanghai, China, in 2016 and 2019, respectively. He is currently pursuing the Ph.D. degree in electromagnetic field and microwave technology with the School of Electronic and Information Engineering, South China University of Technology, Guangzhou, China.

His current research interests include electrically small antennas, mobile terminal antennas, MIMO antennas, 5G antennas, and antenna decoupling.

Mr. Li is currently serving as a Reviewer for IEEE Access and the *Applied Computational Electromagnetics Society (ACES) Journal*.

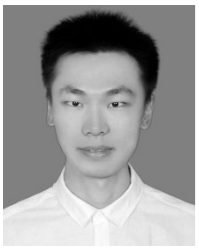

XUGANG ZHANG was born in Henan, China, in 1994. He received the B.S. degree in communication engineering from the Central South University of Forestry and Technology, Hunan, China, in 2016. He is currently pursuing the M.S. degree in circuit and system with the School of Communication and Information Engineering, Shanghai University.

His current research interests include sub-6-GHz MIMO antennas in mobile terminals and the antenna design using machine learning.

WENHUI SHEN was born in Anhui, China, in 1972. He received the B.S. degree in electronic science technology from the Wuhan Institute of Technology, in 1994, the M.S. degree in electronic science technology from the Nanjing University of Post and Telecommunication, in 2000, and the Ph.D. degree in electrical engineering from Shanghai Jiao Tong University, in 2005. In 1999, he was with the Nanjing Institute of Electronic Technology. From 2000 to 2002, he was an Engineer with the Shanghai Design Institute of Post and Telecommunication. He is currently an Associate Professor with Shanghai University. His research interests include microstrip antenna, smartphone antenna, genetic algorithm, and the theory of Maxwellian circuits.